

Multi-axis Force Measurement based on Vision-based Fluid-type Hemispherical Tactile Sensor

Yuji Ito, Youngwoo Kim, *Member, IEEE* and Goro Obinata, *Member, IEEE*

Abstract— We propose a new method for the measurement of multi-axis contact force by using vision-based fluid-type tactile sensor. The proposed sensor can also estimate the multimodal tactile information such as the slippage, the shape, the contact region and the location of the contacted object. Multi-axis contact force is transformed from the elastic membrane tensional force on the touchpad surface, and the touchpad inner pressure measured by the pressure transducer. We obtain the tensional force by solving the equilibrium equations developed in each compartmentalized segment of the membrane, based on the shape information of the touchpad. The proposed method is general and can be applied to various touchpad contact situations. The usefulness of the proposed method is demonstrated through experimental results.

I. INTRODUCTION

Tactile sensing is crucial for robots to adapt to the change of the environment, especially in robot with human-machine interface [1]. In order to control robot hands that are subjected to external forces in a complex manner, contact forces not only in the normal direction for the contact pressure but also in the tangential direction for the shear stress are required. If a robot hand grasps an long object at the end, a moment may occur and thus four-axis force is working at the contact point. However, implementation of the tactile sensors to robot hands is subjected to the external forces that are applied in various directions. Therefore, multi-axis contact force has to be measured for dexterous handling of robot hands.

Many researchers have tried to measure the contact force by using various sensing elements which include resistive, capacitive, piezoelectric, ultrasonic, electromagnetic elements [1]. Micro Electro Mechanical Systems (MEMS)-based sensing elements and cantilevers with resistors have been arrayed to measure two or three dimensional contact force distribution [2]. The sensor reported in [3] estimates three-axis contact force distribution based on the diffusion of the light traveling in the rigid acrylic plate. The light is diffused on the contact region between the acrylic plate and the deformable rubber sheet on the sensor surface. The sensor surface does not deform, since the acrylic plate is rigid. Therefore, it is difficult to ensure sufficient contact areas for stable grasping.

Yuji. Ito is with Graduate School of Engineering, Nagoya University, Furo-cho, Chikusa-ku, Nagoya, 464-8603, Japan (e-mail: ito_yuji@nagoya-u.jp).

Youngwoo. Kim is with Korea Institute of Machinery & Materials (KIMM), Daegu Research Center for Medical Devices and Green Energy, Deagu Techno Park R&D Center #1031, 711 Hosan-dong, Dalseo-gu, 704-948, Korea (e-mail: ywkim@kimm.re.kr).

Goro. Obinata is with EcoTopia Science Institute, Nagoya University, Furo-cho, Chikusa-ku, Nagoya, 464-8603, Japan (e-mail: obinata@mech.nagoya-u.ac.jp).

On the other hand, deformation of the elastic body has been analyzed for the measurement of contact force [4]-[6]. This approach is advantageous because we don't need a large number of sensing elements but only a single elastic body, and also deformation of the elastic body leads to stable contact. K. Kamiyama et al. proposed a three-axis contact force distribution estimation method, where stereoscopic deformation of a flat or finger-shaped sensor body was observed with two-layered arrays of a dotted pattern in the elastic body [4][5]. However, linear deformation of the elastic body with respect to the external force assumed in [4] can be violated by applying a large multi-axis force or under complex situations. The assumption that the sensor is a semi-infinite flat elastic body in [4] cannot be applied to differently-shaped sensor. An experimentally obtained look-up table that describes the relationship between deformation and contact force was used in [5]. However, in particular multi-axis force sensing, constructing the look-up table under various situations requires large data sets. Change of the elastic body's properties such as shape and stiffness needs to reconstruct the look-up table again. Our group proposed a vision-based tactile sensor with an elastic body type touchpad [6]. This sensor measures four-axis contact forces via the look-up table based on the analysis of the displacements of a dotted pattern on the sensor surface. The insufficient look-up table yields large estimation errors in non-ideal conditions that include when objects' contact surface is irregular, when a tangential force and a moment are applied simultaneously on the touchpad surface, and so on.

In this paper, we propose a new method to measure the multi-axis contact force, based on the calculation of the tensional force of the elastic membrane and the inner pressure of the fluid-type tactile sensor. The tensional force is calculated by an efficient method solving the equilibrium equations of the membrane. Differently to the previous methods [4]-[6], the proposed method does not assume linear stress-strain relationship of the elastic material and does not construct look-up table. This means that the proposed method does not depend on the complex elastic property and can be applied to various contact situations. Instead of using an analytical stress-strain relationship of the elastic sensor body, we use inner pressure of the membrane, shape information and contact state of the convex-shaped membrane and sifting directions of printed dots representing the direction of the membrane's tension at the border. The inner pressure can be measured with a general fluid pressure transducer, while the shape and contact state of the membrane can be obtained with the previously developed methods of [7] and [8], respectively. In articles [7]-[9], it was presented that with the developed fluid-type tactile sensor, various tactile information that includes the slippage degree, the shape/irregularity of objects,

the contact region of the sensor and the position/orientation of an object and so on can be accurately measured. Combining the proposed method with the fluid-type sensor, multi-axis contact force can be also measured. The usefulness of the proposed method is confirmed through experimental results.

II. VISION-BASED TACTILE SENSOR FOR MULTIMODAL SENSING

Fig.1 shows the configuration of the vision-based tactile sensor. It consists of a CCD camera, LED lights, a transparent acrylic plate, and touchpad. For the experiments, a CCD camera (TOSHIBA CORPORATION: IK-SM43H) with dimensions $8 \times 8 \times 40$ mm and LED lights dimensioned as $60 \times 60 \times 60$ mm are used. The touchpad has semispherical shape. Its curvature radius is 20 mm and the height is 13 mm. The surface of the touchpad is made of two-layered elastic membrane of silicon rubber (Shin-Etsu Silicone KE-1950-10) as shown in Fig.1. The outer membrane is black, while the inner membrane is white, where each membrane's thickness is 0.5 mm. Translucent red colored water fills the inside of the membrane. Dotted pattern is printed on the inner membrane. In order to make the dotted pattern without impairing the flatness of the membrane, black silicon rubber was applied on the inner membrane, masking the membrane surface except the dotted pattern. Dots have diameter of 0.7 mm and the distance between two neighbor dots of the array is 1.5 mm. The LED source uses a polarized light filter to eliminate the light reflected from the transparent acrylic plate and produces uniform light beam directed in parallel to the image capturing direction. A pressure transducer to measure the inner pressure of the fluid-type touchpad is introduced. The touchpad is connected to the pressure transducer through the elastic tube with its bore diameter of 2 mm, as in Fig.1. The CCD camera takes images of the inner spherical surface of the touchpad through the acrylic plate with sampling frequency of 30 Hz. Fig.2 shows the captured images whose sizes are 640×482 effective pixels. Fig.2 (a) and (b) show the captured image when the sensor is not in contact, and in contact with an object, respectively.

With this sensor, we can obtain many types of tactile information that includes a contact force/moment, the slippage degree, the shape/irregularity of the touchpad/contacted objects, the contact region of the sensor and the position/orientation of the objects [7]-[9]. Analyzing sequential frames of the dotted patterns leads to the estimation of the slippage degree of the object [9], where the slippage degree implies partial slippage in the contact region before macroscopic slippage. The three-dimensional shape of the touchpad can be also calculated by analyzing the intensities of the light color components (red, green and blue) in the captured image [7]. The contact region between the object and the sensor can be obtained based on an analysis of the curvature radius at each point of the touchpad [8]. We can also calculate the object position and orientation by using the positions of the dots on the sensor surface [8].

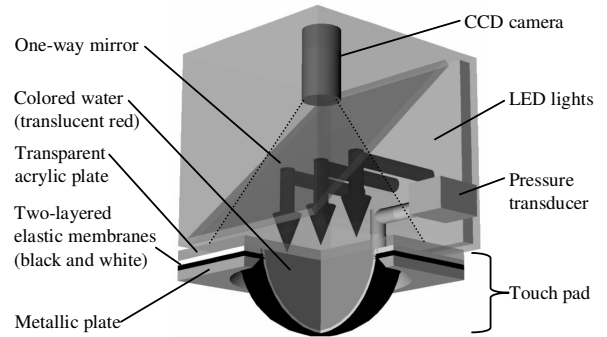


Figure 1. Configuration of vision-based tactile sensor.

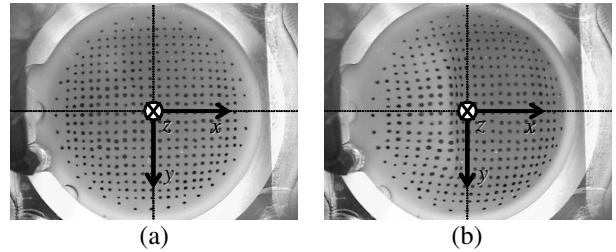


Figure 2. Captured images; (a) non-contact state. (b) contact state.

III. MEASUREMENT OF SIX-AXIS CONTACT FORCE

A. Theory of Contact Force Calculation

As shown in Fig.3, the sensor base is subjected to the tensional force f of the membrane and the inner pressure p of the touchpad. In this study, the volume forces of the membrane and the translucent red water is ignored since they are small enough in comparison with measurable range of forces. The resultant force of the tensional force and the inner pressure gives a six-axis contact force that is being applied to the sensor as follows.

$$\mathbf{F}_{base} = \int f ds + p S_{base} \quad (1)$$

$$\mathbf{M}_{base} = \int \mathbf{l} \times f ds + \int \mathbf{l}_s \times p dS = \int \mathbf{l} \times f ds \quad (2)$$

Here, \mathbf{F}_{base} and \mathbf{M}_{base} are three-axis force vector, and three-axis moment vector, respectively and S_{base} is the area of the sensor base. In Fig.3, Q is defined as the center of S_{base} and is a zero moment point, around which the moment by only the inner pressure on the sensor base is 0. f and p are the tensional force vector of the membrane per unit length and the vector of the inner pressure, respectively. \mathbf{l} , \mathbf{l}_s and S_{base} are the vector from Q to the border of the membrane, the vector from Q to the minute element of S_{base} , dS and the area subjected to the inner pressure, respectively.

When the touchpad doesn't contact an object, \mathbf{F}_{base} and \mathbf{M}_{base} remain at 0. The contact of an object to the touchpad changes f and p , and resultantly yields non-zero \mathbf{F}_{base} and \mathbf{M}_{base} . Now, \mathbf{l} , \mathbf{l}_s and S_{base} in (1) and (2) are obtained from the shape information of the touchpad since the proposed sensor can estimate the touchpad's shape [7]. Therefore, we can

calculate the six-axis contact force F_{base} and M_{base} by acquiring f and p , where the pressure transducer measures p .

B. Outline of Tensional Force Calculation

When the tensional force of the elastic membrane is calculated, it is not straightforward to use the relation between the stress and the strain of the membrane because of the nonlinear characteristics. Therefore, we propose a tensional force estimation method based on the key points; developing the equilibrium equations on each segment of the membrane, representing the direction of the membrane's tension by estimating from the positions of "side dots" printed on the side of the inner membrane as shown later in Fig.6, and solving the equations with iteration method. The calculation process is shown as follows.

Step 1: Compartmentalize the entire membrane into a number of segments, each with a sufficiently small size.

Step 2: Develop the equilibrium equations of each segment in consideration of the tensional forces and the inner pressure.

Step 3: Estimate the directions of the tensional forces at the side of the membrane based on "side dots" printed on the side of the inner membrane.

Step 4: Calculate the resultant tensional forces at the border by solving the equations with iteration method like the Gauss-Seidel method.

The details of each step are described as follows.

C. Step1: Compartmentalization of Membrane

We first define x , y and z axes as shown in Fig.4, where the original point is set to Q , x and y axes are parallel to the acrylic plate, and z axis is vertical to x and y axes. $u(\psi)$ axes on the x - y plane are also defined, where the angle between $u(\psi)$ and x axes is ψ rad. As shown in Fig.4, the contour lines $A(j)$ ($j = 1, 2, \dots$) are introduced on the membrane at every constant minute interval δ_z . The n points $B_s(i)$ ($i = 1, 2, \dots, n$) are equiangularly set that lie at the border of the membrane on the $u(2\pi/n)$ axis. Here, n is a constant parameter. The n lines $B(i)$ ($i = 1, 2, \dots, n$) are drawn on the membrane from $B_s(i)$ such that they are perpendicular to each $A(j)$. When $B(i)$ is drawn from $B_s(i)$, there exists a point at which the inclination of $B(i)$ on x - y plane is 0. This point is defined as $B_g(i)$. Here, the segment enclosed by the lines $A(j)$, $A(j+1)$, $B(i)$ and $B(i+1)$ is defined as the segment $M(i, j)$. In similar way, the line $A_g(i)$ that connects $B_g(i)$ and $B_g(i+1)$ is defined. The segment enclosed by the lines $A(m(i))$, $A_g(i)$, $B(i)$ and $B(i+1)$ is defined as the segment $M(i, m(i))$, where $m(i)$ is determined such that $A_g(i)$ is higher than $A(m(i))$ in z direction but lower than $A(m(i)+1)$. $M(n, j)$ ($j = 1, 2, \dots, m(i)-1$) is enclosed by the lines $A(j)$, $A(j+1)$, $B(n)$ and $B(1)$. Similarly $M(n, m(n))$ is enclosed by the lines $A(m(i))$, $A_g(n)$, $B(n)$ and $B(1)$.

D. Step2: Equilibrium Equations of Each Segment

First, a segment-dependent orthonormal basis $X(i, j)$ - $Y(i, j)$ - $Z(i, j)$ is defined, where $Z(i, j)$ axis is parallel to z axis. When $S_X(i, j)$, $S_Y(i, j)$ and $S_Z(i, j)$ are defined as the projected areas of $M(i, j)$ on the planes vertical to the $X(i, j)$, $Y(i, j)$ and $Z(i, j)$

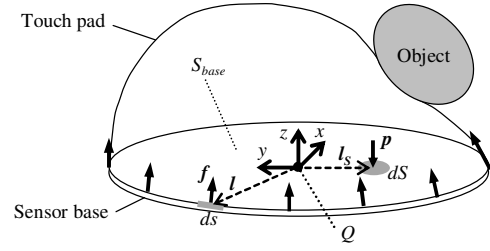


Figure 3. Balance between tensional force of membrane and inner pressure of touchpad.

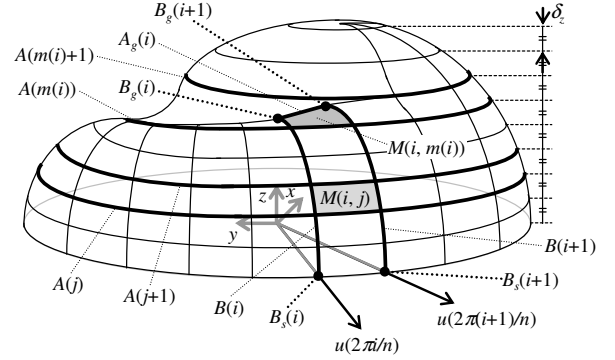


Figure 4. Compartmentalization of membrane.

axes, respectively, the direction of $X(i, j)$ axis is determined such that $S_X(i, j)$ is minimized as in Fig.5 (b). $S(i, j)$ is defined as the vector whose X , Y and Z direction components are $[S_X(i, j), S_Y(i, j), S_Z(i, j)]$. We define the normal tensional force vectors and the shear force vectors at the borders of each segment as shown in Fig.5. $f_v(i, j)$, $f_h(i, j)$, $f_v(i, j+1)$ and $f_h(i+1, j)$ are the tensional forces normal to each boundary lines to the adjoining segments. $\tau_v(i, j)$, $\tau_h(i, j)$, $\tau_v(i, j+1)$ and $\tau_h(i+1, j)$ are the shear forces parallel to the borderlines. The X , Y and Z direction components of f_v , f_h , τ_v and τ_h are defined as $[f_{vX}, f_{vY}, f_{vZ}]$, $[f_{hX}, f_{hY}, f_{hZ}]$, $[\tau_{vX}, \tau_{vY}, \tau_{vZ}]$ and $[\tau_{hX}, \tau_{hY}, \tau_{hZ}]$. The stress at each boundary of the segment is assumed to be evenly-distributed because of small size of each segment. The points of application of f_v , f_h , τ_v and τ_h are at the centers of the boundaries of each segment.

Note that the integral of f in (1) and (2) can be represented with the sum of $f_v(i, 1)$ and $\tau_v(i, 1)$ ($i = 1, 2, \dots, n$), which are the normal tensional and shear forces at the side of the membrane. Therefore, by defining $F_v(i)$ as the resultant force of $f_v(i, 1)$ and $\tau_v(i, 1)$ in (3), (1) and (2) are transformed into (4) and (5).

$$F_v(i) \equiv f_v(i, 1) + \tau_v(i, 1) = n_d(i) \sqrt{|f_v(i, 1)|^2 + |\tau_v(i, 1)|^2} \quad (3)$$

$$F_{base} \equiv \sum_{i=1}^n F_v(i) + pS_{base} \quad (4)$$

$$M_{base} \equiv \sum_{i=1}^n l(i) \times F_v(i) \quad (5)$$

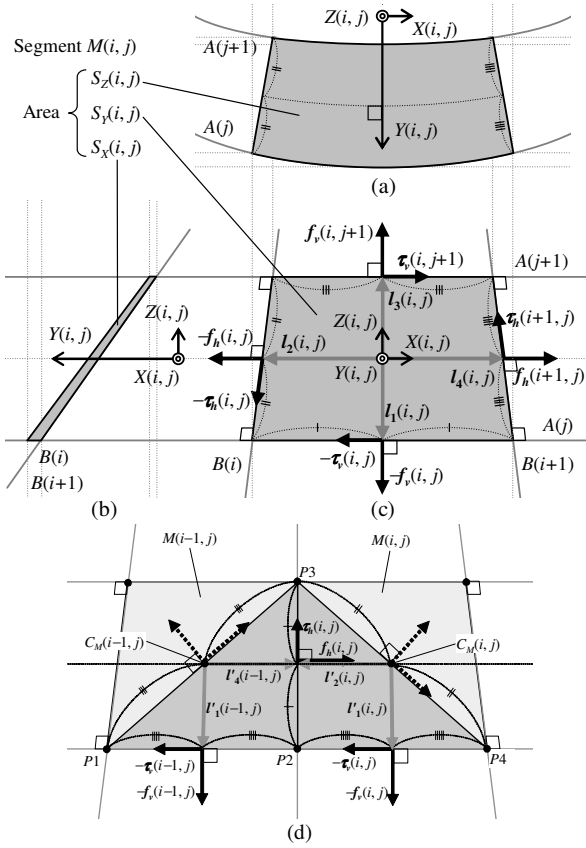


Figure 5. Balance of segment $M(i, j)$ on the membrane; (a) Segment viewed from $X(i, j)$ - $Y(i, j)$ plane. (b) Segment viewed from $Y(i, j)$ - $Z(i, j)$ plane. (c) Segment viewed from $X(i, j)$ - $Z(i, j)$ plane. (d) Triangle segments $P_1P_2P_3$ and $P_2P_3P_4$.

, where $\mathbf{n}_d(i)$ is the unit directional vectors of $\mathbf{F}_v(i)$. Therefore, we can acquire the six-axis contact force \mathbf{F}_{base} and \mathbf{M}_{base} by calculating $f_v(i, 1)$ and $\tau_v(i, 1)$.

In order to obtain $f_v(i, 1)$ and $\tau_v(i, 1)$, the equilibrium equations of the segments are introduced. When $M(i, j)$ is not in contact with an object, the $X(i, j)$, $Y(i, j)$ and $Z(i, j)$ -directional equilibrium equations of $M(i, j)$ are given as follows

$$\begin{aligned} & -f_v(i, j) + f_v(i, j+1) - f_h(i, j) + f_h(i+1, j) \\ & -\tau_v(i, j) + \tau_v(i, j+1) - \tau_h(i, j) + \tau_h(i+1, j) \\ & + pS(i, j) = 0 \end{aligned} \quad (6)$$

, where p is the inner pressure. When the $Y(i, j)$ directional component of vector \mathbf{a} is defined as $[\mathbf{a}]_{Y(i, j)}$, the moment balance of $M(i, j)$ at its weighted center around $Y(i, j)$ axis is expressed by the following equation

$$\begin{bmatrix} -\tau_v(i, j) \times L_1(i, j) - \tau_h(i, j) \times L_2(i, j) \\ + \tau_v(i, j+1) \times L_3(i, j) + \tau_h(i+1, j) \times L_4(i, j) \end{bmatrix}_{Y(i, j)} = 0 \quad (7)$$

, where $L_1(i, j)$ and $L_2(i, j)$, $L_3(i, j)$ and $L_4(i, j)$ are the moment arm vectors from the weighted center of $M(i, j)$ to $\tau_v(i, j)$, $\tau_h(i, j)$, $\tau_v(i, j+1)$ and $\tau_h(i+1, j)$ as shown in Fig.5 (c), respectively. As shown in Fig.5 (d), the moment balances of the triangle segments $P_1P_2P_3$ and $P_2P_3P_4$ at $C_M(i-1, j)$ and $C_M(i, j)$ around

$Y(i-1, j)$ and $Y(i, j)$ axis, respectively, are given by the following equations

$$\begin{cases} \left[\begin{array}{l} \tau_h(i, j) \times L'_4(i-1, j) + m_{ps}(i-1, j) \\ - \{f_v(i-1, j) + \tau_v(i-1, j)\} \times L'_1(i-1, j) \end{array} \right]_{Y(i-1, j)} \cong 0 \\ \left[\begin{array}{l} - \{f_v(i, j) + \tau_v(i, j)\} \times L'_1(i, j) \\ - \tau_h(i, j) \times L'_2(i, j) + m_{ps}(i, j) \end{array} \right]_{Y(i, j)} \cong 0 \end{cases} \quad (8)$$

, where $m_{ps}(i-1, j)$ and $m_{ps}(i, j)$ are the moment vector by the inner pressure around $C_M(i-1, j)$ and $C_M(i, j)$ applied to the triangle segments $P_1P_2P_3$ and $P_2P_3P_4$, respectively. Next, the equilibrium equations for a set of some adjoining segments are considered. Since (6), (7) and (8) are satisfied when the segments are not in contact with objects, $m'(i)$ is defined such that the segments $M(i, 1)$ to $M(i, m'(i))$ are not in the contact region and $M(i, m'(i)+1)$ is in the contact region. The proposed sensor can achieve this selection by applying the contact region estimation method presented in [8]. By substituting 1, 2, 3, ... $m'(i)$ into j in (6) in turn, we also develop the following equations.

$$\begin{aligned} f_v(i, 1) &= f_v(i, m'(i)+1) - \tau_v(i, 1) + \tau_v(i, m'(i)+1) \\ &+ \sum_{j=1}^{m'(i)} \left\{ \begin{array}{l} -f_h(i, j) + f_h(i+1, j) \\ -\tau_h(i, j) + \tau_h(i+1, j) + pS(i, j) \end{array} \right\} \end{aligned} \quad (9)$$

Here, geometric consideration of the segment allows us to show that some elements of \mathbf{f} and $\boldsymbol{\tau}$ become 0. When viewed from $X(i, j)$ - $Z(i, j)$ plane in Fig.5 (c), the line $A(j)$ is parallel not only to the direction of $\tau_v(i, j)$ but also to the direction of $f_h(i, j)$ because the line $B(i)$ is perpendicular to both of $A(j)$ and $f_h(i, j)$. Since the line $A(j)$ is vertical to $Z(i, j)$ axis, the $Z(i, j)$ directional components of $\tau_v(i, j)$ and $f_h(i, j)$ are 0 as follows.

$$\begin{cases} \tau_{vz}(i, j) = 0 \\ f_{hz}(i, j) = 0 \end{cases} \quad (10)$$

$f_h(i, m(i))$ is also vertical to $Z(i, m(i))$ axis because the inclinations of lines $B(i)$ and $B(i+1)$ at $B_g(i)$ and $B_g(i+1)$ are 0 on the x - y plane, as shown in Fig.4. This satisfies the following equation.

$$f_{vz}(i, m(i)+1) = 0 \quad (11)$$

Now, i_0 is defined such that the segments $M(i_0, 1)$ to $M(i_0, m(i_0))$ are not in the contact region. By substituting (10) and (11) into (9), we can simplify the $Z(i, j)$ -directional equilibrium equation as follows.

$$f_{vz}(i_0, 1) = \sum_{j=1}^{m(i_0)} \{ -\tau_{hz}(i_0, j) + \tau_{hz}(i_0+1, j) + pS_z(i_0, j) \} \quad (12)$$

E. Step3: Estimation of Tensional Forces Directions based on Side Dots

In order to understand the boundary condition of the membrane, the directions of the tensional forces $\mathbf{n}_d(i)$ in (3) are required. We introduce the side dots printed on the side of the inner membrane at regular intervals as shown in Fig.6. The

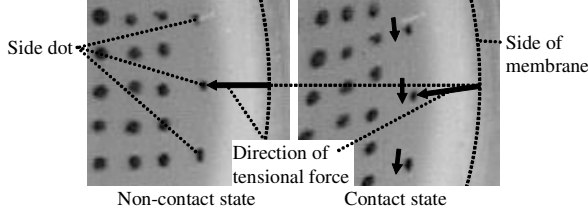


Figure 6. Side dots representing direction of tentional force.

three-dimensional position of side dots represent the direction of the tension of the membrane. Therefore, we estimate the direction of $\mathbf{n}_d(i)$ based on the vector from the side of the membrane to the three-dimensional position of the side dot.

F. Step4: Calculation of Tensional Forces with Iteration Method

Since the proposed sensor can obtain each segment's shape by applying the method presented in [7], the directions of all forces $\mathbf{f}_v, \mathbf{f}_h, \boldsymbol{\tau}_v, \boldsymbol{\tau}_h$, and the projected areas of segments S_x, S_y, S_z are can be calculated. If one directional component in each force is acquired, the other directional components are determined. Therefore, unknowns are only the force's magnitudes $|\mathbf{f}_v|, |\mathbf{f}_h|, |\boldsymbol{\tau}_v|$ and $|\boldsymbol{\tau}_h|$.

In this section, we iterate the following process to solve the simultaneous equilibrium equations and to calculate the resultant tensional forces $\mathbf{f}_v(i, 1)$ and $\boldsymbol{\tau}_v(i, 1)$. First, the beginning values to $\boldsymbol{\tau}_v$ and $\boldsymbol{\tau}_h$ are assigned as follows.

$$\begin{cases} |\boldsymbol{\tau}_v(i, j)| \cong |\boldsymbol{\tau}_v(i, j+1)| \\ |\boldsymbol{\tau}_h(i, j)| \cong |\boldsymbol{\tau}_h(i+1, j)| \end{cases} \quad (13)$$

It is considered that this beginning values in (13) are close to the true values of them because of the shear forces' small sizes and symmetrical distribution. We can obtain $f_{vz}(i_0, 1)$ by substituting (13) into (12). Substituting $f_{vz}(i_0, 1)$ and (13) into (6) yields $f_{vj}(i_0, j)$ ($j = 2, 3, \dots, m(i_0)+1$) in order of increasing j . With the obtained $f_{vj}(i_0, j)$, solving the simultaneous equations of (6) with (13) yields $f_{hj}(i_0, j)$ ($j = 1, 2, \dots, m(i_0)+1$). Similarly we obtain $f_{hj}(i, j)$ ($i = 1, 2, \dots, n, j = 1, 2, \dots, m'(i)+1$) by substituting $f_{hj}(i_0, j)$ and (13) into (6). Finally, all unknown values of $f_{vj}(i, 1)$ ($i = 1, 2, \dots, n$) are determined by substituting $f_{hj}(i, j)$ and (13) into (9).

After acquisition of $f_{vj}(i, 1)$ and $\mathbf{n}_d(i)$ estimated by side dots in Section III.E, we can calculate $\boldsymbol{\tau}_v(i, 1)$ by substituting $f_{vj}(i, 1)$ and $\mathbf{n}_d(i)$ into (3). And substituting $\boldsymbol{\tau}_v(i-1, 1)$ and $\boldsymbol{\tau}_v(i, 1)$ into (8) yields $\boldsymbol{\tau}_h(i, 1)$ ($i = 1, 2, \dots, n$). We obtain $\boldsymbol{\tau}_h(i, 2)$ ($i = 1, 2, \dots, n$) by substituting $\boldsymbol{\tau}_h(i, 1), \boldsymbol{\tau}_h(i, 1)$ and $\boldsymbol{\tau}_h(i+1, 1)$ into (7). $\boldsymbol{\tau}_h(i-1, 2)$ and $\boldsymbol{\tau}_h(i, 2)$ are substituted into (8) to obtain $\boldsymbol{\tau}_v(i, 2)$ for all i and substituting them into (7) yields $\boldsymbol{\tau}_h(i, 3)$ for all i . In similar way, $\boldsymbol{\tau}_v(i, j)$ and $\boldsymbol{\tau}_h(i, j)$ of non-contact segments are obtained in order of increasing j .

Next, we recalculate the $f_{vj}(i, 1)$ by substituting the obtained $\boldsymbol{\tau}_h(i, j)$ into (12). By iterating this process until the convergence of $f_{vj}(i, 1), f_{vj}, f_{hj}, \boldsymbol{\tau}_v$ and $\boldsymbol{\tau}_h$ are acquired and the six-axis forces \mathbf{F}_{base} and \mathbf{M}_{base} from (4) and (5) are finally obtained.

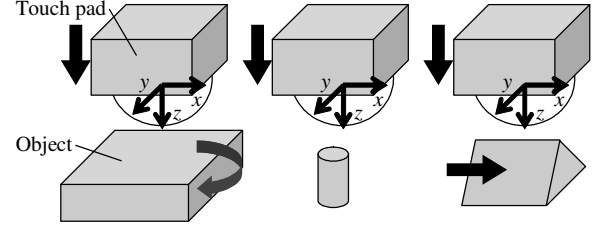


Figure 7. Experimental methods shown in chapter IV.

IV. EXPERIMENTAL RESULTS

In order to confirm the usefulness of the proposed method for multi-axis contact force measurement, some experiments were conducted. Based on the coordinate system of Fig.4, we define x, y and z -directional forces as F_x, F_y and F_z , respectively, and moments around z -axes as M_z , respectively. When forces and moments were applied to the touchpad, and the proposed method measured them. True values of the applied forces were obtained by additionally installed commercial force sensor whose the rated outputs of F_x, F_y, F_z and M_z are 25 N, 25 N, 50 N and 0.15 Nm, respectively. Their linearity error and hysteresis are smaller than 1.0 % of the rated outputs. A constant interval δ_z and the number of points n in section III.C were set to 0.2 mm and 72, respectively.

The speed of the processor used in the PC is 2.66 GHz (Intel(R) Core(TM)2 Duo E6750 processor). The image processing tool (MVTec: HALCON 10) is used. Computation rate of the proposed method is about 1.0 Hz at present.

In the following sections, we show the experimental results, where the touchpad contacts with flat, cylinder-shaped and triangular pole-shaped objects as in Fig.7.

A. Measurement of Normal Force

The normal force F_z was measured when the touchpad was in contact with some objects in z direction as in Fig.7. Fig.8 compares the measured value and actual value of F_z , where dots on the black line represent the measured and actual values are quite identical with each other. The external force was applied to the touchpad and increased it from 0 N to 28 N, 22 N and 15 N when the touchpad contacts flat, cylinder-shaped and triangle pole-shaped objects, respectively. The ranges of the external forces are determined based on the size of the contact region. We found that F_z is well measured for various shaped objects and the maximum error of F_z is 2.70 N (9.5 % of the full scale 28.26 N). It is considered that the measurement error is mostly comes from the touchpad shape-sensing error by using the method in [7].

B. Measurement of Normal and Tangential Forces

While moving in x -direction the object that was contacting with the touchpad, the tangential force F_x and the normal force F_z were measured. Fig.9 shows the measured values of F_x and F_z when the touchpad contacts with the triangle pole-shaped object. The result of Fig.9 shows that the proposed method can measure the normal force and the tangential force simultaneously, where maximum measurement error of F_z is

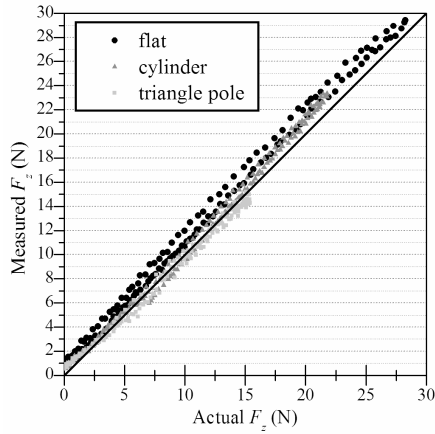


Figure 8. Measured value of the normal force F_z .

1.99 N (7.0 % of the full scale 28.26 N). Although measurement error of F_x is temporarily 1.53 N (19.7 % of the full scale 7.79 N), mean absolute error of F_x is 0.545 N (7.00 % of the full scale 7.79 N). It is considered that the measurement error of F_x depends on the measurement errors of F_z and the directions of $\mathbf{n}_d(i)$ invoked by the estimated shape.

C. Measurement of Normal Force and Rotational Moment in the Horizontal Plane

The moment M_z around z -axis and normal force F_z were simultaneously measured while rotating the object that is contacting the touchpad. Fig.10 shows the measured value of M_z and F_z when the touchpad is contacting the flat object. The experiment was continued until the contacted object made macroscopic slippage. It is considered that the measurement error of M_z depends on the measurement errors of F_z and the directions of $\mathbf{n}_d(i)$. In Fig.10, the maximum errors of M_z and F_z are smaller than 0.0177 Nm and 0.92 N, respectively, which are 13.1 % and 3.26 % of the full scales (0.1357 Nm and 28.26 N). However, the proposed method measures the normal force and the moment simultaneously in Fig.10.

V. DISCUSSION AND FUTURE WORK

We have proposed a new method to measure the multi-axis contact force, based on the calculation of the tensional force of the elastic membrane and the inner pressure of the fluid-type tactile sensor. The proposed method does not depend on the complex elastic property and can be applied to various contact state since linearity assumption of stress-strain relationship of the elastic material and look-up table is not used. The usefulness of the proposed method was confirmed through experiments.

Although the computational time is not short enough for online processing, we believe the proposed method can achieve real-time performance by optimizing the program for the method and/or implementing itself in fast processing units such as field-programmable gate array (FPGA) and graphics processing units (GPU). Future work includes the implementation of the developed sensor to a robot hand.

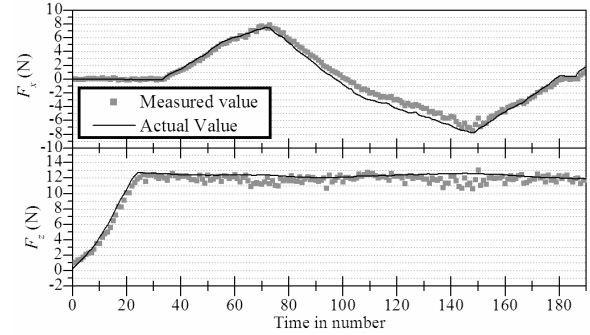


Figure 9. Measured value of the tangential force F_x with the normal force F_z .

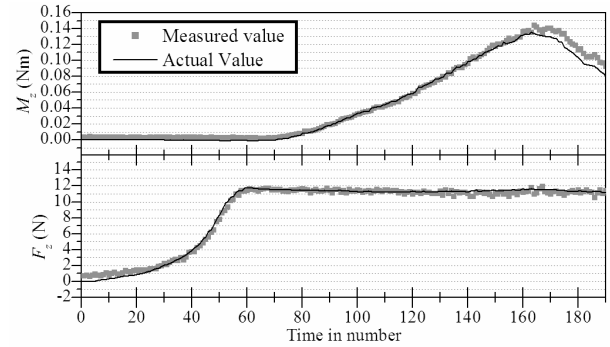


Figure 10. Measured value of the moment M_z with the normal force F_z .

REFERENCES

- [1] R.S. Dahiya, G. Metta, M. Valle, G. Sandini "Tactile Sensing—From Humans to Humanoids" *IEEE Trans. on Robotics*, Vol. 26, No. 1, pp. 1-20, Feb, 2010.
- [2] C. Wen and W. Fang, "Tuning the sensing range and sensitivity of three axes tactile sensors using the polymer composite membrane", *The Sensors and Actuators A: Physical*, Vol. 145-146, pp. 14-22, 2008.
- [3] M. Ooka, "Optical Three-axis Tactile Sensor" *Mobile Robots: Perception & Navigation*, pp. 111-136, 2007.
- [4] K. Kamiyama, K. Vlack, T. Mizota, H. Kajimoto, N. Kawakami and S. Tachi, "Vision-Based Sensor for Real-Time Measuring of Surface Traction Fields" *IEEE Computer Graphics and Applications*, Vol.25, No.1, pp. 68-75, Jan-Feb, 2005.
- [5] K. Sato, K. Kamiyama, H. Nii, N. Kawakami and S. Tachi, "Measurement of Force Vector Field of Robotic Finger using Vision-based Haptic Sensor", *In Proceedings of the 2008 IEEE/RSJ International Conference on Intelligent Robots and Systems*, pp. 488-493, 2008.
- [6] G. Obinata, D. Ashis, N. Watanabe and N. Moriyama, "Vision Based Tactile Sensor Using Transparent Elastic Fingertip for Dexterous Handling" *Mobile Robots: Perception & Navigation*, pp. 137-148, 2007.
- [7] Y. Ito, Y. Kim, C. Nagai and G. Obinata, "Vision-based Tactile Sensing and Shape Estimation Using a Fluid-type Touchpad", *IEEE Trans. on Automation Science and Engineering*, Vol.9, Issue.4, pp. 734-744, 2012.
- [8] Y. Ito, Y. Kim, C. Nagai and G. Obinata, "Contact State Estimation by Vision-based Tactile Sensors for Dexterous Manipulation with Robot Hands Based on Shape-Sensing", *International Journal of Advanced Robotic Systems*, Vol.8, No.4, pp. 225-234, 2011.
- [9] Y. Ito, Y. Kim and G. Obinata, "Robust Slippage Degree Estimation based on Reference Update of Vision-based Tactile Sensor", *IEEE Sensors Journal*, Vol.11, Issue.9, pp. 2037-2047, 2011